# Type-II $Bi_2O_2Se/MoTe_2$ van der Waals Heterostructure Photodetectors with High Gate-Modulation Photovoltaic Performance

Dan, Zhiying; Yang, Baoxiang; Song, Qiqi; Chen, Jianru; Li, Hengyi; Gao, Wei; Huang, Le; Zhang, Menglong; Yang, Mengmeng; Zheng, Zhaoqiang

*Published in:*
ACS Applied Materials and Interfaces

*DOI:*
10.1021/acsami.3c01807



*Publication date:*
2023

ACS APPLIED MATERIALS & INTERFACES

www.acsami.org

Research Article

# Type-II $Bi_2O_2Se/MoTe_2$ van der Waals Heterostructure Photodetectors with High Gate-Modulation Photovoltaic Performance

Zhiying Dan, Baoxiang Yang, Qiqi Song, Jianru Chen, Hengyi Li, Wei Gao,* Le Huang, Menglong Zhang, Mengmeng Yang, Zhaoqiang Zheng, Nengjie Huo, Lixiang Han,* and Jingbo Li*

Cite This: *ACS Appl. Mater. Interfaces* 2023, 15, 18101−18113

Read Online

ACCESS | Metrics & More | Article Recommendations | Supporting Information

**ABSTRACT:** In recent years, two-dimensional (2D) nonlayered $Bi_2O_2Se$-based electronics and optoelectronics have drawn enormous attention owing to their high electron mobility, facile synthetic process, stability to the atmosphere, and moderate narrow band gaps. However, 2D $Bi_2O_2Se$-based photodetectors typically present large dark current, relatively slow response speed, and persistent photoconductivity effect, limiting further improvement in fast-response imaging sensors and low-consumption broadband detection. Herein, a $Bi_2O_2Se$/2H-$MoTe_2$ van der Waals (vdWs) heterostructure obtained from the chemical vapor deposition (CVD) approach and vertical stacking is reported. The proposed type-II staggered band alignment desirable for suppression of dark current and separation of photoinduced carriers is confirmed by density functional theory (DFT) calculations, accompanied by strong interlayer coupling and efficient built-in potential at the junction. Consequently, a stable visible (405 nm) to near-infrared (1310 nm) response capability, a self-driven prominent responsivity ($R$) of 1.24 A·W$^{-1}$, and a high specific detectivity ($D^*$) of 3.73 × 10$^{11}$ Jones under 405 nm are achieved. In particular, $R$, $D^*$, fill factor, and photoelectrical conversion efficiency (PCE) can be enhanced to 4.96 A·W$^{-1}$, 3.84 × 10$^{12}$ Jones, 0.52, and 7.21% at $V_g$ = −60 V through a large band offset originated from the n$^+$−p junction. It is suggested that the present vdWs heterostructure is a promising candidate for logical integrated circuits, image sensors, and low-power consumption detection.

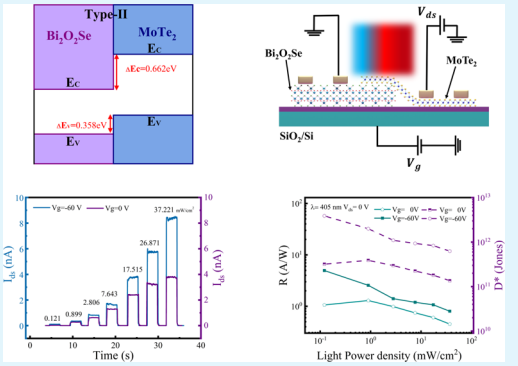


**KEYWORDS:** *$Bi_2O_2Se$, 2H-$MoTe_2$, 2D van der Waals heterostructure photodetector, type-II band alignment, gate-modulation photovoltaic effect*



## 1. INTRODUCTION

To date, atomically thin two-dimensional (2D) materials including graphene and transition metal dichalcogenides (TMDs) have exhibited tremendous potential applications in next-generation spintronics, polarization-sensitive detection, optical communication, imaging sensor, and neuromorphic computing, attributing to their dangling-bond free surface, thickness-dependent physics, strong light−matter interaction, and various confined structures.[1−3] In particular, 2D optoelectronics based on individual components are typically insufficient for handling the trade-off between ultra-fast response speed and high responsivity ($R$) owing to the prolonged photocarrier lifetime caused by the defect levels or filled trapping centers at high carriers' concentration.[4] For instance, Hong et al. reported an active pixel image sensor array with a bilayer $MoS_2$ film. Although the maximum $R$ of the phototransistor can reach 119.16 A·W$^{-1}$, the rise/decay time at $V_{ds}$ = 5 V and $V_g$ = −35 V are as slow as 119/122 ms under 405 nm excitation due to the S vacancy.[5] Moreover, narrow-band-gap materials such as multilayered black phosphorus (BP) and tellurium possess a large dark current of 10$^{-6}$−10$^{-4}$ A at $V_{ds}$ = 1 V, resulting in low sensitivity, slow response speed, and high noise interference.[6,7] Alternatively, localized field enhancement is an efficient strategy to modulate the optoelectrical performance, but it may lead to high power consumption, limited spectrum response, unexpected operation problems, and multiple stacking process. Fortunately, a 2D van der Waals (vdWs) junction provides a valid platform to pursue high sensitivity, fast response speed, broadband spectrum absorption, and high specific detectivity ($D^*$) of the photodetector.[8−10] Regardless of lattice matching, diverse materials' family, and flexible stacking architecture, a type-II band alignment vdWs heterojunction can be designed to form

Received: February 8, 2023
Accepted: March 22, 2023
Published: March 29, 2023

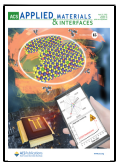

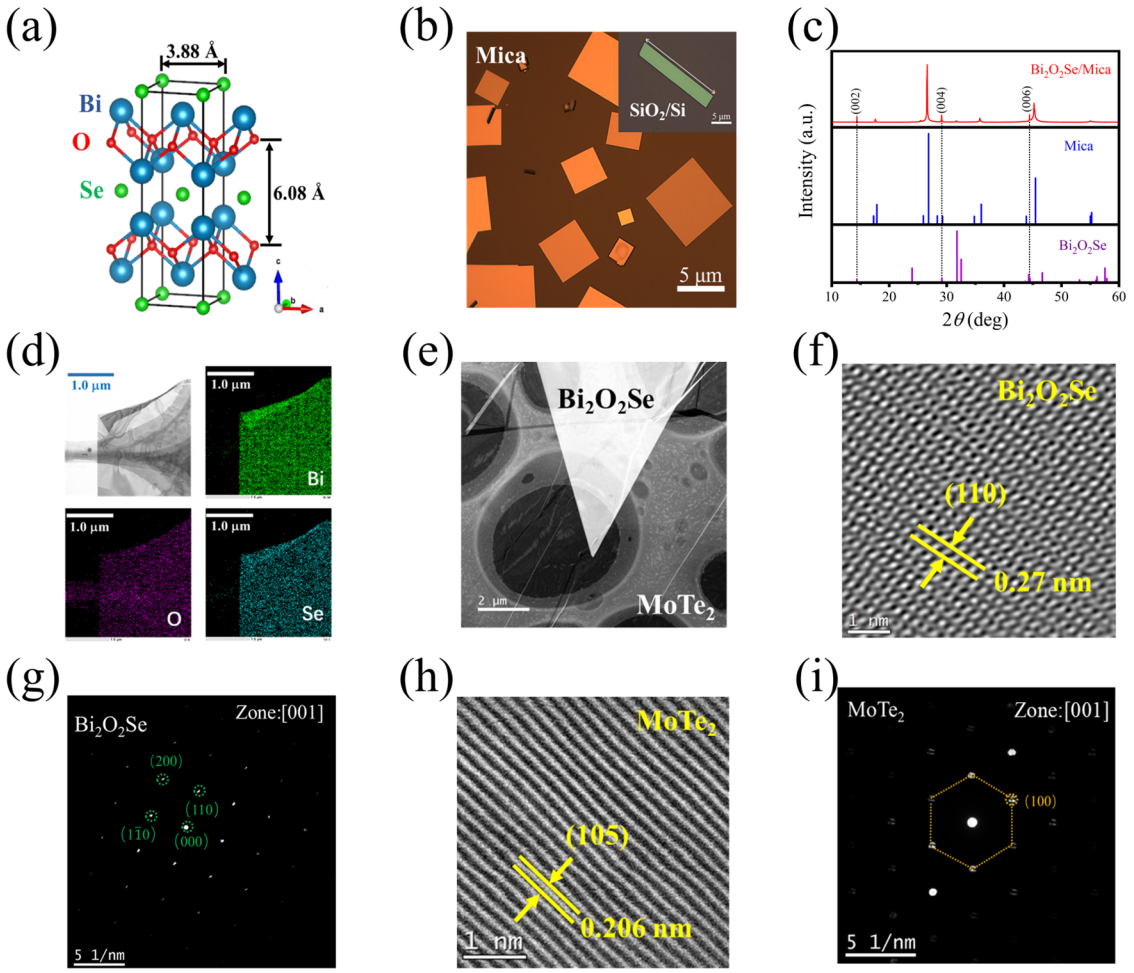


**Figure 1.** Characterization of $Bi_2O_2Se$ nanoplates and the $MoTe_2/Bi_2O_2Se$ heterostructure: (a) Schematic illustration of the crystal structure of $Bi_2O_2Se$ with a tetragonal structure. (b) Typical OM image of the as-synthesized $Bi_2O_2Se$ nanoplates on mica, the inset is an OM image of 2D $Bi_2O_2Se$ nanoplates after being transferred to $SiO_2/Si$. (c) XRD patterns of $Bi_2O_2Se$ nanoplates grown on mica (red), mica substrate (blue), and a reference of $Bi_2O_2Se$ (violet). (d) The low-resolution TEM and EDS elemental mapping for Bi, O, and Se. (e) $Bi_2O_2Se/MoTe_2$ heterojunction on a Cu grid. (f) HRTEM image of the $Bi_2O_2Se$ nanoplate, indicating a d-spacing of 0.27 nm for (110) planes. (g) The SAED pattern of $Bi_2O_2Se$ NSs suggests its single crystallinity. (h) HRTEM image of the $MoTe_2$ nanoplate. (i) The SAED pattern of $MoTe_2$ NSs suggests their single crystallinity.

an effective built-in potential barrier to generate and separate photoinduced carriers under photovoltaic and photoconductive mode with or without gate voltage.[11] Meanwhile, distinct advantages of individual components, strong interlayer coupling effect, and efficient intralayer transition will also lead to tunable multifunctions, wider spectrum response, ultrashort photoluminescence lifetime, and unique charge transport mechanism. For example, Fang et al. fabricated a type-II 2D $Cs_2AgBiBr_6/WS_2$/graphene heterostructure-based photodetector.[12] The large energy offset reveals efficient electron transport between a $Cs_2AgBiBr_6$ light absorption layer and monolayer $WS_2$. As a result, a maximum $R$ of 0.52 A·W$^{-1}$, a high $D^*$ of $1.5 \times 10^{13}$ Jones, and a fast response speed of 52.3/53.6 $\mu$s can be achieved with a graphene electrode under 455 nm illumination.

In 2017, as an intriguing ternary semiconductor, 2D $Bi_2O_2Se$ composed of $(Bi_2O_2)_{2n+}$ and $(Se)_{2n-}$ through a layer-by-layer electrostatic force with an interlayer spacing of 0.608 nm, was successfully synthesized by Peng et al.[13] Instead of the mechanical exfoliation method, large-scale, high-quality, and atomically thin $Bi_2O_2Se$ nanosheets can be obtained by the chemical vapor deposition (CVD) method. Furthermore, atmosphere-stable $Bi_2O_2Se$ possesses a narrow band gap of 0.8 eV, a high Hall mobility of 20,000 cm$^2$ V$^{-1}$ s$^{-1}$ at 2 K, a broadband spectrum response of 360−1600 nm, a high on/off ratio of >10$^6$, and so on. Recently, Li et al. first observed Shubnikov-de Hass oscillations and linear magnetoresistance of >500% in Se-poor $Bi_2O_2Se$.[14] Nevertheless, because of high carrier concentrations of $10^{18}$−$10^{20}$ cm$^{-3}$ and an intrinsic bolometric effect, typical $Bi_2O_2Se$-based photodetectors exhibit a large dark current of >$10^{-6}$ A, a small $I_{light}/I_{dark}$ ratio (<10), relatively slow or unstable response speed, and persistent photoconductive behavior. Although they can be alleviated via a precise controllable synthetic process and top-gate modulation, they will impede the potential application in large-scale facile manufacture and fast-speed imaging regions. In recent years, with the fast development of polymer transfer technology, several $Bi_2O_2Se$ nanosheets with high quality can be entirely isolated from mica to overcome the interfacial electrostatic force to construct 2D/2D, 2D/three-dimensional (3D) vdWs heterojunctions or other structures, leading to the improved properties and the exploration of novel functional devices such as memristors, THz-detection, phototransistors, resistance switching, photonic integrated circuits, and thermoelectrics.[15−17] As for $Bi_2O_2Se$/3D vdWs heterostructures, Wu et al. transferred $Bi_2O_2Se$ onto a silicon waveguide, resulting in


https://doi.org/10.1021/acsami.3c01807
ACS Appl. Mater. Interfaces 2023, 15, 18101−18113

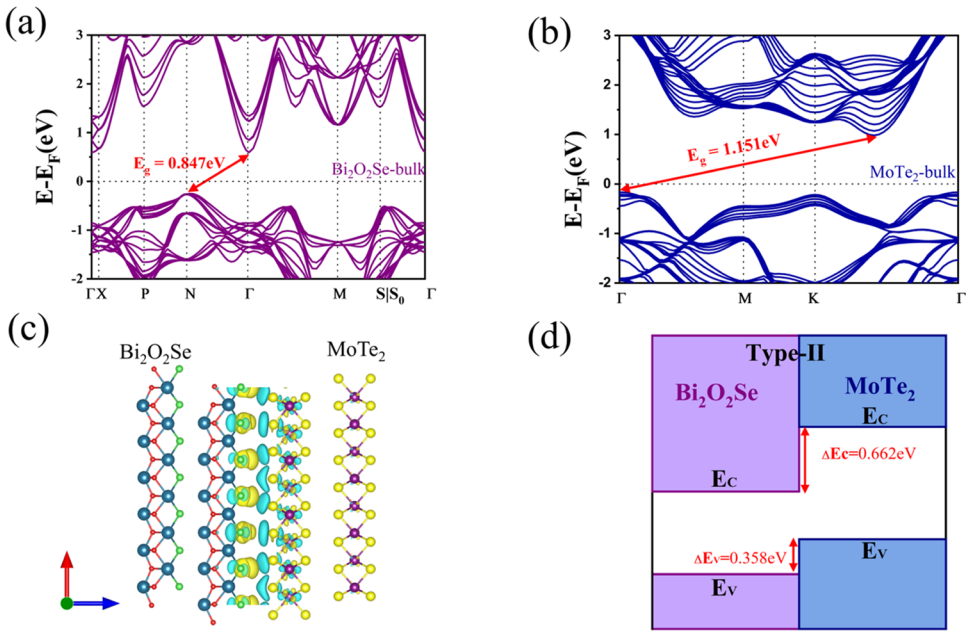


**Figure 2.** Calculated band structures using the HSE method based on first-principles calculations: (a) Band structures of bulk $Bi_2O_2Se$. (b) Band structures of bulk 2H-$MoTe_2$. (c) 3D isosurface of the charge density difference across the $Bi_2O_2Se/MoTe_2$ interface. (d) Schematic of the band diagram of the $Bi_2O_2Se/MoTe_2$ heterojunction before contact.

a small dark current of 72.9 nA, a high $R$ of 3.5 $A{\cdot}W^{-1}$, a fast rise/decay time of 22/78 ns, and a low noise-equivalent power of 15.1 $pW{\cdot}Hz^{-0.5}$ at a $V_{ds}$ of 2 V for communication applications.[18]

Meanwhile, in terms of $Bi_2O_2Se$/2D vdWs heterostructures, 2D materials with ambipolar conducting behavior composed of $WSe_2$ and BP have been integrated with $Bi_2O_2Se$ to suppress the dark current, broaden the spectrum, and facilitate the response speed. In 2021, a type-I $Bi_2O_2Se$/BP vdWs-based broadband photodetector with a high $R$ of 4.3 $A{\cdot}W^{-1}$ at 1310 nm and a response time of 9 ms was investigated by Liu et al.[6] However, atmosphere-unstable BP and a relatively low rectification ratio of 20 also limit further applications. In contrast, Luo et al. developed a type-II $Bi_2O_2Se/WSe_2$ vdWs heterostructure with a broadband capability from 365 to 2000 nm by constructing efficient charge separation and strong interlayer coupling.[19] But a photovoltaic $R$ of 284 $mA{\cdot}W^{-1}$ under 532 nm is less prominent. Up to now, another atmosphere-stable ambipolar material, namely, 2H-$MoTe_2$, exhibits an indirect band gap range of 0.80−1.15 eV and a strong bias voltage-tunable conductivity behavior from p-type to ambipolar-type to n-type conducting behavior depending on the thickness.[20−22] However, the theoretical band alignment calculation, characterization, and electrical and optoelectrical performances have not been reported yet for the $Bi_2O_2Se/MoTe_2$ heterostructure.

Herein, $Bi_2O_2Se$ with high crystalline quality is successfully synthesized on f-mica by the CVD method. Meanwhile, the electronic structures of bulk $Bi_2O_2Se$ and bulk $MoTe_2$ are calculated. As expected, the corresponding charge density difference conducted via the HSE06 method confirmed a type-II staggered-type band alignment. Subsequently, a multilayered $Bi_2O_2Se/MoTe_2$ vdWs vertical heterojunction is fabricated on the $SiO_2/Si$ substrate via the nondestructive transfer and manual stacking method. Benefiting from the high light absorption efficiency of $Bi_2O_2Se$, effective built-in electric field, and strong interlayer coupling at the $Bi_2O_2Se/MoTe_2$ interface, the device achieves a low dark current in the order of ∼0.9 pA at zero bias, accompanied by a moderate rectification ratio of $10^2$. Meanwhile, a significant ambipolar conducting behavior can be achieved with an $I_{on}/I_{off}$ ratio of $10^3$. Under illumination, it shows a stable and continuous self-driven photoswitching from 405 to 1310 nm. In particular, the maximum $R$ is as high as 1.24 $A{\cdot}W^{-1}$ and the corresponding $D^*$ can reach $3.73 \times 10^{11}$ Jones, indicating a strong photoresponse for the $n^+$−n junction under 405 nm irradiation. Furthermore, an $n^+$−p junction can be realized at $V_g = -60$ V to enlarge the built-in potential difference. As a result, the maximum $R$, $D^*$, fill factor (FF), and PCE are enhanced to 4.96 $A{\cdot}W^{-1}$, $3.84 \times 10^{12}$ Jones, 0.54, and 7.21%, respectively, with a fast response time of 157/141 $\mu$s. At last, the broadband self-driven performance of the heterojunction from visible to infrared light (405−1310 nm) was explored, among which $R$ and $D^*$ were 19 $mA{\cdot}W^{-1}$ and $5.72 \times 10^9$ Jones at 1310 nm, respectively. The above results suggest that the promising $Bi_2O_2Se/MoTe_2$ vdWs heterojunction delivers a potential application in solar cells and visible−near-infrared imaging systems.

## 2. RESULTS AND DISCUSSION

2D $Bi_2O_2Se$ nanosheets were constructed on freshly cleaved f-mica [$KMg_3(AlSi_3O_{10})F_2$] substrates by the CVD method.[23,24] $Bi_2O_2Se$ consists of alternative compensating cations ($(Bi_2O_2)^{2n+}_n$) and anions ($Se^{2n-}_n$). As displayed in Figure 1a, the layers are held together by weak electrostatic forces with an interlayer spacing of about 0.608 nm along the $c$-axis.[25] Figure 1b shows the morphology of synthetic $Bi_2O_2Se$ on f-mica through optical microscopy (OM), in which the sample presents square or rectangular shapes. The inset displays one of the selected rectangular samples for heterostructure construction that transferred from f-mica onto a 300 nm $SiO_2/Si$ substrate by a polystyrene (PS)-assisted transfer method. In Figure 1c, three orientation peaks located at 14.47, 29.21, and 44.51° correspond to the lattice


https://doi.org/10.1021/acsami.3c01807
ACS Appl. Mater. Interfaces 2023, 15, 18101−18113

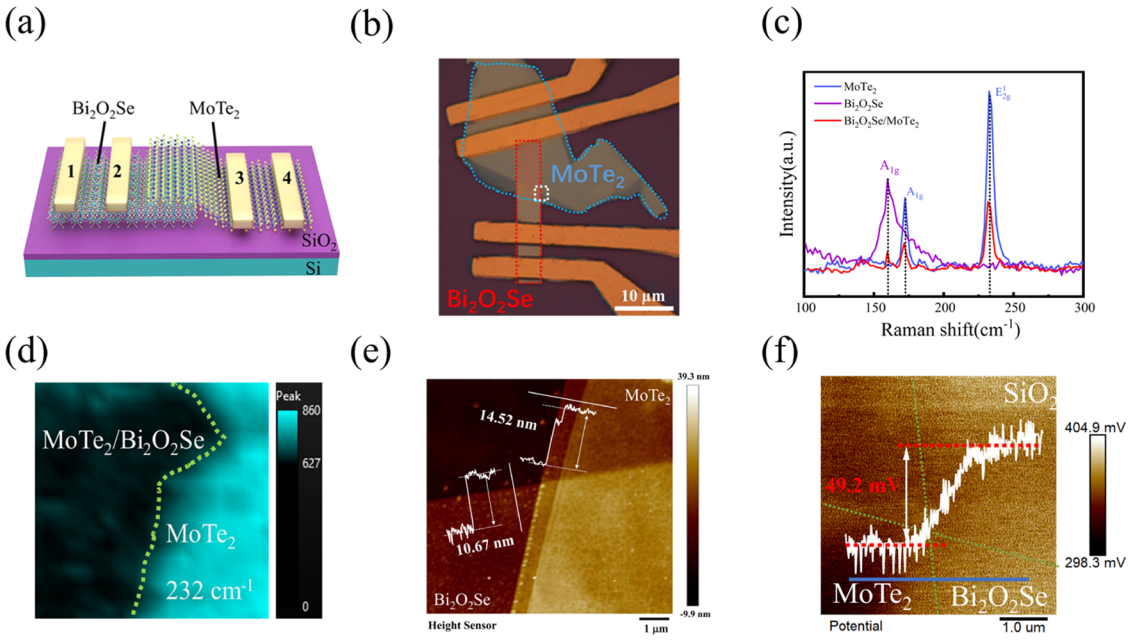


**Figure 3.** Characteristics of the $Bi_2O_2Se/MoTe_2$ heterojunction device: (a) 3D schematic of the $Bi_2O_2Se/MoTe_2$ heterojunction device. (b) The corresponding optical image of the fabricated $MoTe_2/Bi_2O_2Se$ heterostructure. (c) Normalized Raman spectrum of bare $Bi_2O_2Se$, $MoTe_2$, and its heterojunction. (d) Raman mapping peak of 232 $cm^{-1}$ for $MoTe_2$, in the white rectangle of (b). (e) The atomic force microscopy (AFM) image of $MoTe_2$ and $Bi_2O_2Se$. (f) KPFM image of the $Bi_2O_2Se/MoTe_2$ heterojunction. The inset shows the potential profile along the blue line.

planes of (002), (004), and (006) with a tetragonal phase of $Bi_2O_2Se$ (JCPDS = No.73-1316).[26] To further investigate the single-crystal nature and tetragonal structure of $Bi_2O_2Se$ nanoflakes, high-resolution transmission electron microscopy (HRTEM) and selected area electron diffraction (SAED) patterns are introduced. The energy-dispersive spectroscopy (EDS) mapping is displayed in Figure 1d, which further confirms the uniform chemical composition distribution of Bi, O, and Se elements. Figure 1e presents a low-magnification TEM image of the heterostructure on the copper grid transferred by the polymethyl methacrylate (PMMA) wet transfer method. As depicted in Figure 1f, the HRTEM image shows clear lattice fringes, suggesting a single-crystal form for the $Bi_2O_2Se$ constituent. The lattice spacing of 0.27 nm can be assigned to the (110) plane. The SAED pattern shows the spots of (200), (110), and $(1\bar{1}0)$ in Figure 1g, which is consistent with the $I_4/mmm$ space group of *c*-axis [001]-oriented $Bi_2O_2Se$.[16] The HRTEM image (Figure 1h) and the corresponding SAED pattern (Figure 1i) show the good single crystallinity and hexagonal structure of exfoliated 2H-$MoTe_2$ in this heterostructure.[27] Above all, our OM, X-ray diffraction (XRD), HRTEM, and EDS results reflect the high crystal quality of the as-prepared $Bi_2O_2Se$, $MoTe_2$ nanosheets, and heterostructure feasibility.

In theory, band alignment is crucial for a heterojunction, as it dictates the migration of charge carriers near the interface. In general, the band structure, theoretical charge density difference, and band alignment of $Bi_2O_2Se/MoTe_2$ could be demonstrated by the first-principles calculation based on density functional theory (DFT). The specific calculated details are demonstrated in the Supporting Information. In Figure 2a, bulk $Bi_2O_2Se$ exhibits a narrow indirect band gap of 0.847 eV, with its valence band maximum (VBM) located at the *N* point and its conduction band minimum (CBM) located on the Γ point. Similarly, bulk $MoTe_2$ also possesses an indirect energy band structure with a moderate band gap of 1.151 eV, and its VBM is located at the Γ point, while its CBM is located along the Γ-K line, as shown in Figure 2b. To check whether charge transfer occurs at the interface, it is necessary to further investigate the charge redistribution $\Delta\rho(z)$ at the time of interface formation. Here, the $x-y$ plane-averaged charge densities $\Delta\rho(z)$ are adopted for calculating $\Delta\rho(z) = \rho_{MolSe}(z) - \rho_{Mo}(z) - \rho_{Se}(z)$. $\rho_{Mo}(z)$, $\rho_{Se}(z)$, and $\rho_{MolSe}(z)$ specify the charge densities of monolayer 2H-$MoTe_2$, $Bi_2O_2Se$, and $Bi_2O_2Se/MoTe_2$ heterobilayer in the same configuration. As depicted in Figure 2c, $\Delta\rho(z)$ is localized at the interface. The charge accumulation ($\Delta\rho(z) > 0$) mainly occurs at the interface close to $Bi_2O_2Se$, while the $MoTe_2$ layer is depleted from electrons ($\Delta\rho(z) < 0$) and becomes positively charged. The sign of the interface dipole is consistent with the changes in the $Bi_2O_2Se$ work function upon contact with the $MoTe_2$ layer. These results will predict the excellent optoelectrical properties of the $Bi_2O_2Se/MoTe_2$ vdWs heterostructure. In addition, the band offsets of $\Delta E_C$ and $\Delta E_V$ are calculated to be 0.662 and 0.358 eV, respectively. Based on this, a type-II energy band arrangement of the $Bi_2O_2Se/MoTe_2$ heterojunction can be concluded, as shown in Figure 2d, which can collect and facilitate the photogenerated carrier separation without a potential barrier and prevent intralayer nonradiative recombination at thermodynamic equilibrium. Their Fermi level difference will be confirmed by Kelvin probe force microscopy (KPFM) measurement.

To verify the theoretical prediction, a multilayered $Bi_2O_2Se/MoTe_2$ vdWs heterostructure is fabricated by the polystyrene (PS) and poly(vinyl alcohol) (PVA) dry transfer method. Figure 3a exhibits a three-dimensional (3D) scheme of the field-effect transistor (FET) based on the $Bi_2O_2Se/MoTe_2$ heterojunction. Four electrodes are designed to test the individual channel (1−2, 3−4 pairs) and the heterojunction channel (2−3 pairs). Figure 3b demonstrates the OM image of the $MoTe_2/Bi_2O_2Se$ heterojunction device with four Cr/Au electrodes. The area surrounded by the blue dashed line


https://doi.org/10.1021/acsami.3c01807
ACS Appl. Mater. Interfaces 2023, 15, 18101−18113

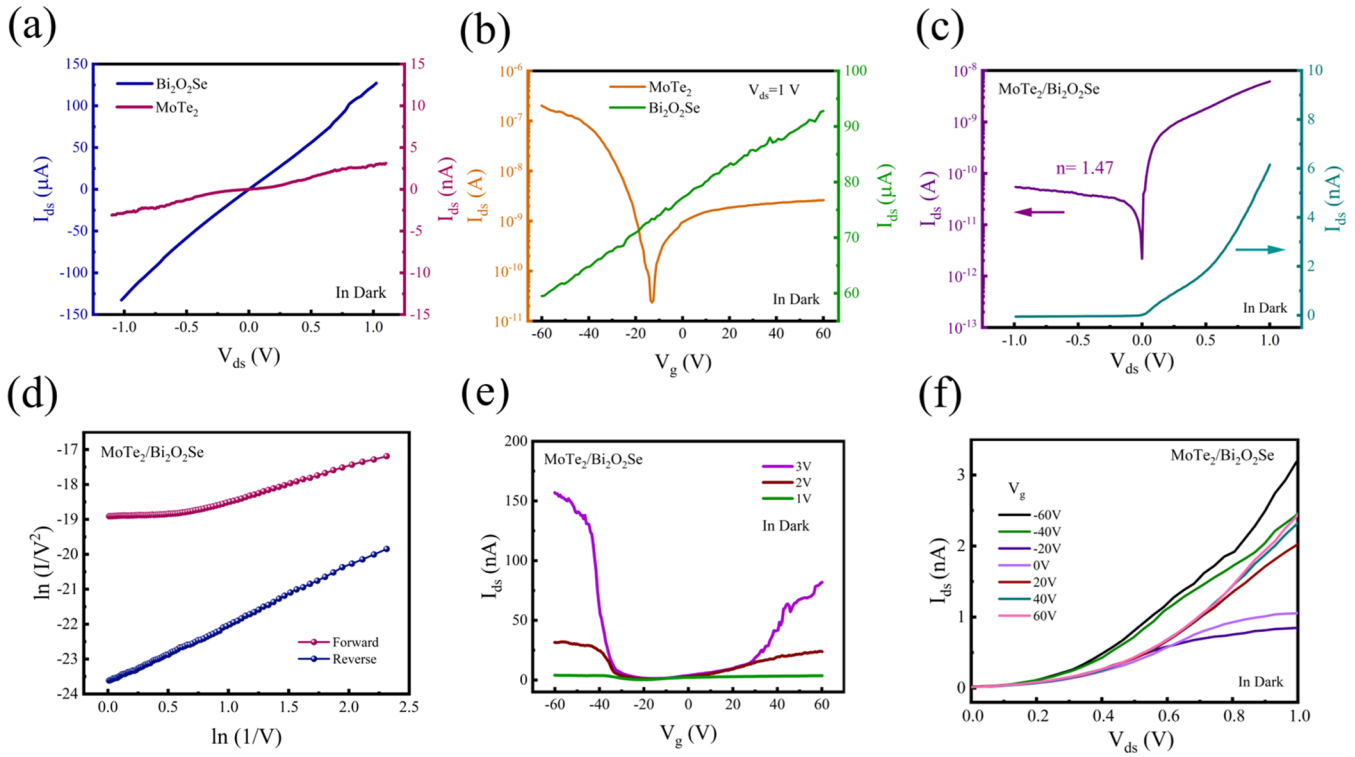


**Figure 4.** Electrical performance of $Bi_2O_2Se/MoTe_2$ vdWs FET: (a) $I_{ds}-V_{ds}$ curves of $Bi_2O_2Se$ and $MoTe_2$ at $V_g = 0$ V. (b) The transfer curves of the $Bi_2O_2Se$ and $MoTe_2$ FET. (c) $I_{ds}-V_{ds}$ curves of $Bi_2O_2Se/MoTe_2$ vdWs FET at $V_g = 0$ V. (d) Direct tunneling (DT) plot extracted from the $I_{ds}-V_{ds}$ curves in (c). (e) The transfer curves of $Bi_2O_2Se/MoTe_2$ FETs. (f) The output curves of $Bi_2O_2Se/MoTe_2$ in the $V_g$ range of −60−60 V at a step of 20 V.

represents exfoliated 2H-$MoTe_2$; in contrast, the CVD-grown rectangular $Bi_2O_2Se$ is labeled in red. Raman spectra of $Bi_2O_2Se$, $MoTe_2$, and the overlapped junction are illustrated in Figure 3c. For $Bi_2O_2Se$ (blue line), a sharp peak at 159 $cm^{-1}$ could be attributed to the out-of-plane $A_{1g}$ vibration mode.[17] For multilayer $MoTe_2$ (black line), two vibration Raman peaks appear at 172 and 232 $cm^{-1}$, corresponding to the as-known out-of-plane $A_{1g}$ and in-plane $E^1_{2g}$ phonon modes, respectively.[28] For the $Bi_2O_2Se/MoTe_2$ overlapped region (red line), all characteristic peaks of $Bi_2O_2Se$ and $MoTe_2$ can be observed. In particular, the less intensive peaks can be attributed to "Raman quenching" across the heterojunction, as a consequence of strong interlayer coupling effects.[29] In addition, a slight red shift of the $A_{1g}$ peak position of $Bi_2O_2Se$ in the heterojunction is due to the effect of electron doping, suggesting that the individual component in the heterojunction was not contaminated after the PS and PVA dry transfer process.[30] As shown in Figure 3d, the Raman mapping of $MoTe_2$ at 232 $cm^{-1}$ further intuitively confirms the uniform distribution, homogeneity, and intensity reduction for the component and the overlapped region in the white rectangle from Figure 3b.

Next, the synchronous atomic force microscopy (AFM) image in Figure 3e confirms the thickness of $Bi_2O_2Se$ and $MoTe_2$ nanosheets in this device, which are about 10.67 nm (16 layers) and 14.52 nm (19 layers) with a smooth and clean surface, respectively.[31] The surface potential difference (SPD) at the $Bi_2O_2Se/MoTe_2$ interface is harvested by Kelvin probe force microscopy (KPFM) measurement. The corresponding calculation details are provided in the Supporting Information. Figure 3f displays the SPD mapping between the $MoTe_2/Bi_2O_2Se$ heterojunction and the Pt/Ir coating KPFM tip. $\Delta E_F$ or the built-in potential difference is calculated to be 49.2 meV, and the depletion width is about 1 $\mu$m as extracted from the potential file along the blue line. It indicates that the electric potential of $Bi_2O_2Se$ was higher than that of $MoTe_2$, and the built-in electric field is pointed from $Bi_2O_2Se$ to $MoTe_2$. Meanwhile, UPS measurements are also carried out, and the results are shown in Figure S3a,b. The work functions ($W_F$) of $MoTe_2$ and $Bi_2O_2Se$ were determined to be about 4.83 and 4.78 eV, respectively, by subtracting the second electron cutoff energy from the photo energy of the He I light source (21.21 eV). The valence band edges of $MoTe_2$ and $Bi_2O_2Se$ were determined to be 0.64 and 0.82 eV, respectively, which are lower than their Fermi level ($E_F$; binding energy equals 0 eV). 50 meV is slightly different from KPFM's results, probably due to the adsorption of small molecules on the surface of the sample during the KPFM test, resulting in a low value.

To investigate the electrical properties of the above $Bi_2O_2Se/MoTe_2$ heterostructure, voltammetric measurements of the transistor are carried out in the darkness at room temperature. At first, the symmetric linear characteristics of the $I_{ds}-V_{ds}$ curves in Figure 4a illustrate the Ohmic contact formed between the Cr/Au electrode and individual $MoTe_2$ and $Bi_2O_2Se$. In particular, the output curves of $Bi_2O_2Se$ displayed a heavily n-type characteristic behavior in Figure S4a, and the back-gate modulation is poor. Besides, the output curves of $MoTe_2$ exhibited ambipolar conducting characteristics in Figure S4b. As shown in Figure 4b, the transfer curves at a $V_{ds}$ of 1 V for bare $MoTe_2$ FETs (3−4 electrodes) exhibit a p-dominated ambipolar conducting behavior at $V_g$ scanning from −60 to 60 V. The hole current $I_{on}/I_{off}$ ratio is calculated to be $10^4$, and the electron $I_{on}/I_{off}$ ratio is approximately $10^2$. Thus, the $MoTe_2$ channel can be entirely depleted under back-gate


https://doi.org/10.1021/acsami.3c01807
ACS Appl. Mater. Interfaces 2023, 15, 18101−18113

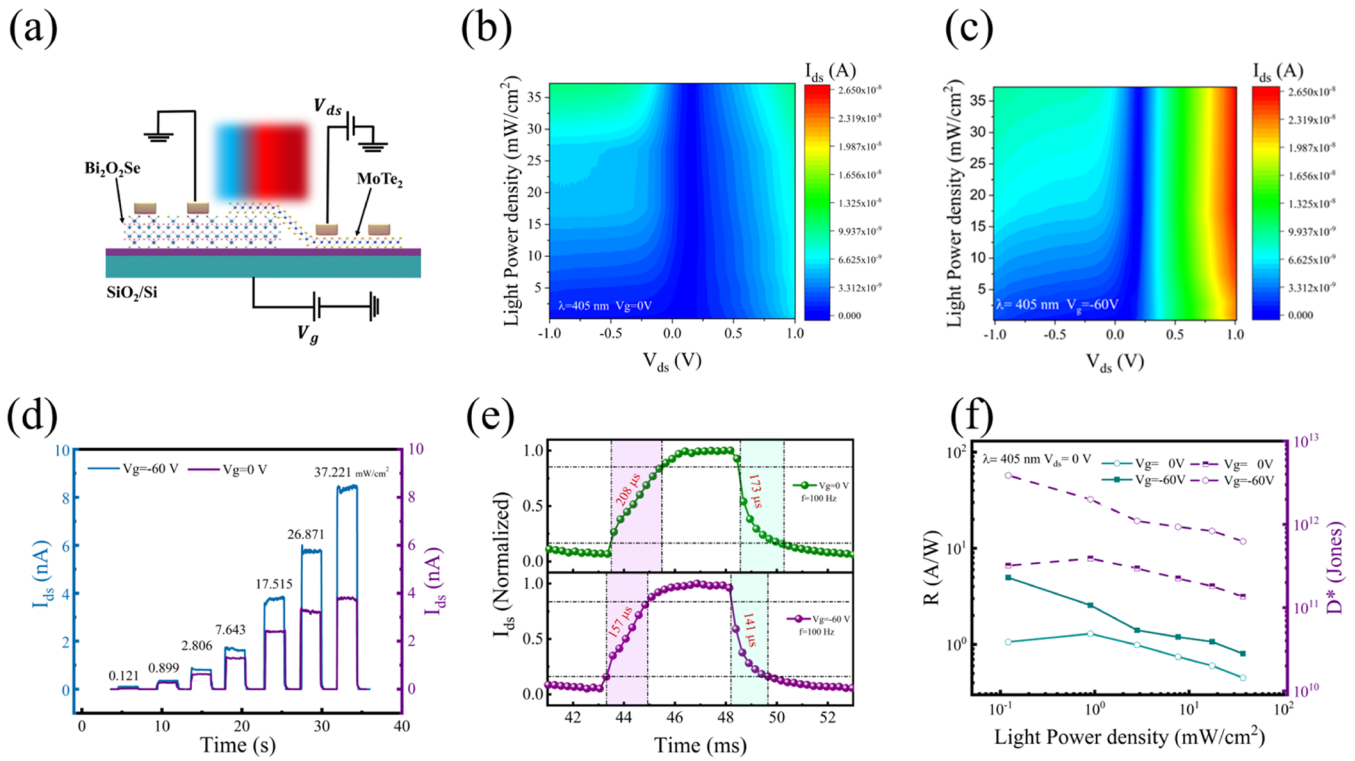


**Figure 5.** Gate-modulation photovoltaic performance of the $Bi_2O_2Se/MoTe_2$ vdWs photodetector under a 405 nm laser: (a) Schematic diagram of the experimental setup for photocurrent measurement. (b) The light power density-dependent photocurrent mapping at $V_g$ = 0 V. (c) The light power density-dependent photocurrent mapping at $V_g$ = −60 V. (d) The time-resolved photoresponse curves of the device under 405 nm illumination with various light power densities at $V_g$ = −60 and 0 V. (e) The dynamic response speed of the device at $V_g$ = −60 and 0 V under 405 nm at $P$ = 37.22 mW cm$^{-2}$. (f) Responsivity and specific detectivity of the device under varying light power densities under 405 nm illumination and $V_g$ = −60 and 0 V.

modulation, and the concentration of electrons ($n$) per unit volume at $V_g$ = 0 V for the individual $MoTe_2$ can be calculated by the following equation:[29]

$$N_n(MoTe_2) = \frac{C_g|V_{th(n)}|}{qt} = 7.79 \times 10^{17}\ cm^{-3}$$

where $q = 1.6 \times 10^{-19}$ C, $C_g = 1.23 \times 10^{-8}$ F cm$^{-2}$ for 300 nm $SiO_2$, and $t$ is the thickness of $MoTe_2$ at around 14.52 nm. The threshold voltage ($V_{th}$) can be extracted based on the extrapolation method, which fits the $V_g$-axis intercept of the linear transfer curve at the first maximum point of the transconductance.[32] As shown in Figure S5, $|V_{th}|$ = 14.73 V for $MoTe_2$ FET in an n-type conducting region. Moreover, the hole or electron field-effect mobilities of $MoTe_2$ were estimated by the following equation:

$$\mu_n(\mu_p) = \frac{dI_{ds}}{dV_g} \times \frac{L}{WC_gV_{ds}} = 0.48(3.58)\ cm^2\ V^{-1}\ s^{-1}$$

where $L$ and $W$ present the length and width across the channel, respectively. However, the $N_n'$ of $Bi_2O_2Se$ cannot be used in the same way. The bare $Bi_2O_2Se$ nanosheet-based device (1−2 electrodes) is difficult to pinch off during the entire $V_g$ scanning from −60 to 60 V, due to the high electron concentration and a narrow band gap of 0.85 eV. Thus, the concentration per unit volume at $V_g$ = 0 V of electrons was calculated by the following equation:

$$N_n'(Bi_2O_2Se) = \frac{\sigma}{\mu_n' \times q} = 7.29 \times 10^{20}\ cm^{-3}$$

where $\mu_n' \approx 70.12$ cm$^2$ V$^{-1}$ s$^{-1}$ is extracted from the transfer curve and $\sigma \approx 8.18 \times 10^3\ \Omega^{-1}cm^{-1}$, according to the output curves at room temperature, as shown in Figure S4a.[29] Thus, an n$^+$-$Bi_2O_2Se$/n-$MoTe_2$ vdWs FET is successfully achieved at $V_g$ = 0 V. The $I_{ds}-V_{ds}$ characteristics of the $Bi_2O_2Se/MoTe_2$-based FET (2−3 electrodes) are measured, as shown in Figure 4c. As expected, a significant diode behavior is observed with a rectification ratio of $1.3 \times 10^2$ at $V_{ds}$ = +1/−1 V originating from the depletion junction. The forward current variation of the $I_{ds}-V_{ds}$ curve can be fitted by using the following Shockley diode equation:[33]

$$I = I_s \exp\left(\frac{qV}{k_BT_n} - 1\right) \quad (1)$$

where $I_s$ is the reverse saturation current, $k_B$ is Boltzmann's constant, and $T_n$ is the absolute temperature. An ideal factor ($n$) of 1.47 (<2) is calculated in this n$^+$−n diode, implying a high-quality interface and diffusion-current domination. Moreover, it is noteworthy that a linear relationship with a positive slope is found in $\ln(I_{ds}/V_{ds}^2)$ against the $\ln(1/|V_{ds}|)$ plot (Figure 4d), which is in good agreement with the direct tunneling (DT) equation.[33] The equation for the DT mechanism is as follows:[34]

$$I_{ds} \propto V_{ds} \exp\left[-\frac{4\pi d\sqrt{2m^*\varphi}}{\hbar}\right] \quad (2)$$

The reduced Planck's constant, tunneling thickness, tunneling barrier, and effective electron mass are given by the characters


https://doi.org/10.1021/acsami.3c01807
ACS Appl. Mater. Interfaces 2023, 15, 18101−18113

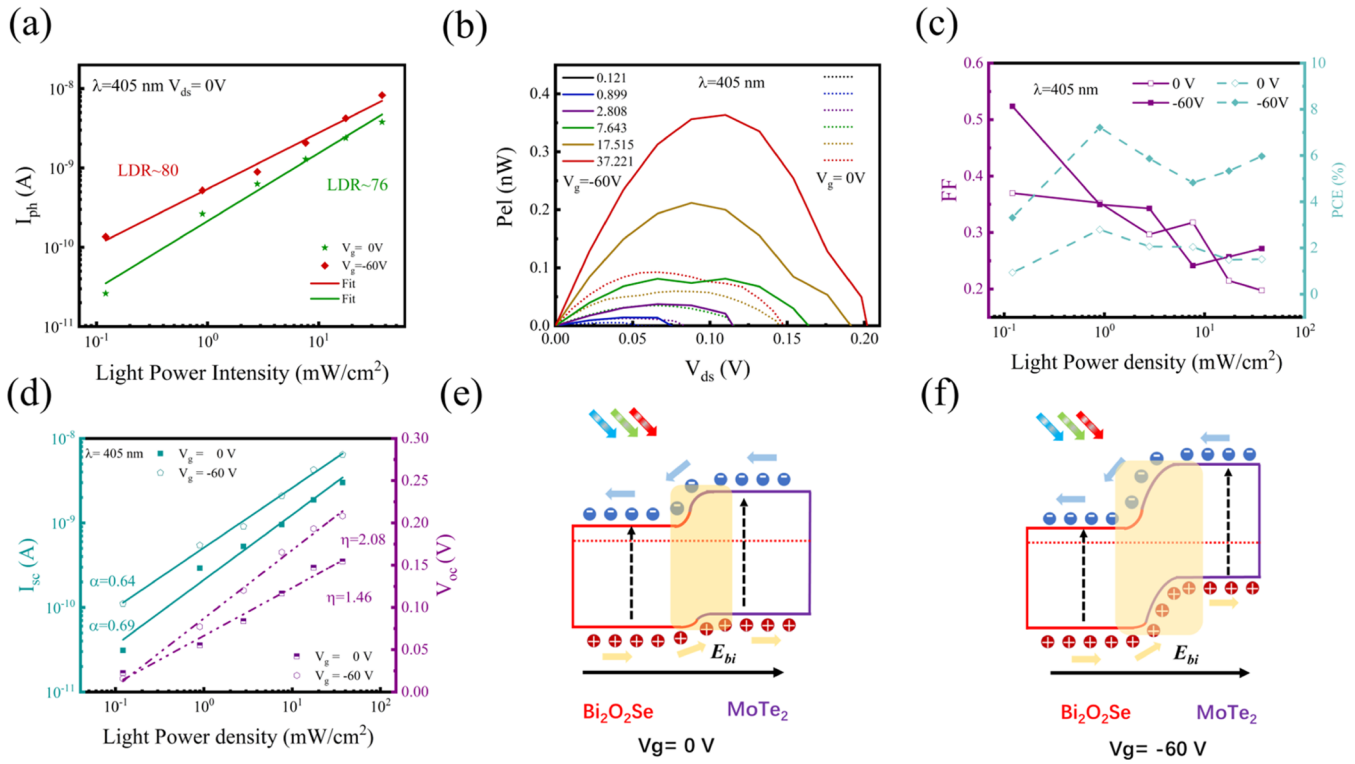


**Figure 6.** Gate-modulation photovoltaic properties and band alignment of the $Bi_2O_2Se/MoTe_2$ vdWs photodetector under 405 nm irradiation: (a) LDR of $Bi_2O_2Se/MoTe_2$ with incident light power intensities ranging from 0.12 to 37.22 mW $cm^{-2}$ at $V_g$ = 0 and −60 V, respectively. (b) Output electrical power generated by the $Bi_2O_2Se/MoTe_2$ heterostructure as a function of $V_{ds}$ under various light power densities. (c) FF and PCE as a function of light power density under 405 nm. (d) Extracted $I_{sc}$ and $V_{oc}$ under different light power densities of 405 nm. (e) Band alignment diagrams of the $Bi_2O_2Se/MoTe_2$ device at $V_g$ = 0 V under light illumination. (f) Band alignment diagrams of the $Bi_2O_2Se/MoTe_2$ device at $V_g$ = −60 V under light illumination.

of $\hbar$, d, $\varphi$, and $m^*$. It can be also reduced to $\ln(I_{ds}/V_{ds}^2)$ versus $\ln(1/|V_{ds}|)$ with a positive slope.

$$\ln\left(\frac{I_{ds}}{V_{ds}^2}\right) \propto \ln\left(\frac{1}{|V_{ds}|}\right) - \frac{4\pi d\sqrt{2m^*\varphi}}{\hbar} \quad (3)$$

This demonstrates that DT is the dominant mechanism rather than F−N tunneling under forward or negative bias. The contribution of DT tunneling current at forward bias is due to the high doping concentration of $Bi_2O_2Se$.[10]

The transfer curves of the $Bi_2O_2Se/MoTe_2$ FET at various $V_{ds}$ values are presented in Figure 4e. Unusually, the hole current $I_{on}/I_{off}$ ratio reaches $1.4 \times 10^2$ at $V_{ds}$ = 1 V. However, as $V_{ds}$ increases from 1 to 3 V, the current $I_{on}/I_{off}$ ratio slightly increases and the ambipolar characteristics become more pronounced. $I_{ds}$ increases with a negative increase in $V_g$ (−20 to −60 V), indicating the entire depletion of holes in the $MoTe_2$ channel, and stabilizes after $V_g$ <−40 V. Meanwhile, an enhancement of $I_{ds}$ is observed against a positive increase in $V_g$ (−20 to 60 V) due to the high electron concentration doping of $Bi_2O_2Se$. Figure 4f shows the output curves corresponding to the heterojunction at different $V_g$ values. Collectively, the devices exhibit p-dominated ambipolar characteristics.

We further provide more insights into the transport mechanism of the $Bi_2O_2Se/MoTe_2$ FET by estimating the depletion widths on the $MoTe_2$ ($x_p$) and $Bi_2O_2Se$ ($x_n$) sides using the following equations:[19]

$$x_p = \sqrt{\frac{2N_n'\varepsilon_2\varepsilon_2 V_{bi}}{qN_p(\varepsilon_1 N_p + \varepsilon_2 N_n')}}, \quad x_n = \sqrt{\frac{2N_p\varepsilon_2\varepsilon_2 V_{bi}}{qN_n'(\varepsilon_1 N_p + \varepsilon_2 N_n')}} \quad (4)$$

where $\varepsilon_1$ and $\varepsilon_2$ are the dielectric constants of $Bi_2O_2Se$ and $MoTe_2$, respectively, and $V_{bi}$ is the built-in potential at the junction. According to the thickness, $\varepsilon_1$ = 20, $\varepsilon_2$ = 10.1,[29] and $V_{bi}$ = 49.2 meV from the AFM-KPFM test results, the calculated $x_n$ is 2.89 nm, and $x_p$ is $5.8 \times 10^{-3}$ nm approximately, indicating that multilayer $Bi_2O_2Se$ and $MoTe_2$ are both undepleted under $V_{ds}$ = 0 V, and the depletion region is mainly located at the $MoTe_2$ side.

As shown in Figure 5a, 400−1550 nm lasers are selected to irradiate vertically and uniformly across the entire channel of the device. Figure 5b illustrates 405 nm illuminated $I_{ds}$ mapping dependent on various light power densities ($P$) from 0.12 to 37.22 mW $cm^{-2}$ at $V_g$ = 0 V. At $V_{ds}$ = 0 V, $I_{ds}$ tends to increase with increasing light power density, verifying the existence of a photovoltaic effect in this $n^+$−n heterojunction. Meanwhile, illuminated $I_{ds}$ at negative and forward $V_{ds}$ is enhanced significantly because of the photoconductive effect's domination. On the one hand, the relationship between $\ln(I/V^2)$ and $\ln(1/V)$ at a forward bias range under illumination can be extracted from Figure 5b, according to eq 3 in Figure S6a. The positive slope of the fitting curves in the whole range indicates the domination of the photoinduced DT effect in the heterojunction. On the other hand, the built-in electric field can be enhanced under negative $V_{ds}$ with the same direction, leading to an increased


https://doi.org/10.1021/acsami.3c01807
ACS Appl. Mater. Interfaces 2023, 15, 18101−18113

photocurrent toward that at $V_{ds}$ = 0 V. Moreover, in the presence of $V_g$ = −60 V, interestingly, the significantly enhanced $I_{ds}$ mapping is monitored, as exhibited in Figure 5c. It is necessary to compare the photovoltaic performance as a function of gate voltage. The intrinsic charge transport mechanism of the gate-modulated photovoltaic behavior will be discussed later.

Intuitively, the time-resolved photovoltaic response curves of the $Bi_2O_2Se/MoTe_2$ heterojunction with and without $V_g$ = −60 V are also investigated in Figure 5d. Noticeably, when $P$ = 37.22 mW cm$^{-2}$, the illuminated $I_{ds}$ monotonously increases from 3.82 to 8.44 nA, and the $I_{light}/I_{dark}$ ratio increases from $6.36 \times 10^3$ to $1.41 \times 10^4$ along with $V_g$ changing from 0 to −60 V at the similar $I_{dark}$ of 0.6 pA. The long-term on/off curves under 405 nm irradiation are measured in Figure S6b,c. After over 300 cycles, the fast and repeatable on/off states indicate the high reliability and reproducibility of $Bi_2O_2Se/MoTe_2$ without spurious photoinduced charge at $V_g$ = 0 and −60 V. Besides, the photoswitching curves under various light power densities at $V_{ds}$ = ±1 V are depicted in Figure S7a,b, also indicating the stable operation process under photoconductive mode.

As the key figures of merit of photodetectors, the response speed ($\tau_{rise}$: photocurrent increases from 10 to 90% of its final value)/decay time ($\tau_{decay}$: photocurrent falls from 90 to 10% of its beginning value), noise, and specific detectivity are also characterized. As displayed in Figure 5e, $\tau_{rise}/\tau_{decay}$ values of 157/141 $\mu$s ($V_g$ = −60 V) and 208/173 $\mu$s ($V_g$ = 0 V) were obtained at a frequency of 100 Hz in Figure S8a−d.[35,36] The Fourier transform of the dark current traces gives the noise spectral density ($S_n$) as a function of frequency, as shown in Figure S9b ($V_g$ = 0 V) and Figure S9d ($V_g$ = −60 V).[4,37,38] At low frequencies, a $1/f$ noise component is observed, attributed to interface traps or defects,[4,37] whereas at high frequencies above 10 Hz, the device reaches a noise floor with very low white noise, about $2 \times 10^{-15}$ A Hz$^{-1/2}$, which is independent of the frequency and close to the scattered particle noise floor. Moreover, at $V_g$ = −60 V, a lower $S_n$ was obtained, probably due to $MoTe_2$ in the heterojunction being electrostatically tuned to P-type doping, creating a larger built-in electric field.

To estimate the level of the photodetection performance for $Bi_2O_2Se/MoTe_2$, key factors such as $R = I_{ph}/PA$ and $D^* = R\sqrt{A/S_n}$ were calculated,[39−42] where $A$ is the effective area of the photodetector and $S_n$ is the noise spectral density. Considering the fast speed of the device, $S_n$ can be extracted at a frequency of 20 Hz. Figure 5f demonstrates the curves of $R$ as a function of $P$ with and without a $V_g$ of −60 V. In general, the $R$-value shows an overall decreasing trend as the $P$ increases.[32] This phenomenon can be attributed to the gradual filling of the trap states at the junction interface with increasing light power density, weakening the Auger recombination probability of photogenerated carriers.[43] It is worth noting that $R$ and $D^*$ reach to their maximum values of 4.96 A W$^{-1}$ and $3.84 \times 10^{12}$ Jones under $V_g$ = −60 V and $P$ = 0.12 mW cm$^{-2}$, respectively.

Based on the ultra-high photoresponse switching ratio of the photodetector, the linear dynamic range (LDR) at $V_{ds}$ = 0 V is further analyzed.[7] In general, the LDR characterizes the light power density range of a photodetector with a constant $R$, which can be given as follows:

$$\mathrm{LDR} = 20 \log\left(\frac{I_{ph}}{I_{dark}}\right) \quad (5)$$

where $I_{ph}$ and $I_{dark}$ represent the photocurrent and dark current at a maximum $P$ of 37.22 mW cm$^{-2}$, respectively. As shown in Figure 6a, the LDR can be enhanced from 76 to 80 dB at $V_g$ = −60 V, which is superior to previously reported 2D photodetectors.[44] Under illumination, the accumulation of photogenerated carriers in the $Bi_2O_2Se$ and $MoTe_2$ layers breaks the equilibrium state, creating a forward open-circuit voltage ($V_{oc}$). Besides, in the short-circuit state of the device, the separated photogenerated electrons and holes move to the opposite electrodes and form a short-circuit current ($I_{sc}$) under the built-in electric field. The output electrical power ($P_{el}$) generated by the $Bi_2O_2Se/MoTe_2$ device at various $P$ is extracted from the equation $P_{el} = I_{ds}V_{ds}$.[45] As depicted in Figure 6b, the maximum $P_{el}$ reaches 0.1 nW and 0.36 nW at $V_g$ = 0 and −60 V, respectively. Furthermore, considering that photoelectric conversion efficiency (PCE) and fill factor (FF) are key quality factors for photovoltaic solar cells, $\mathrm{PCE} = P_{el}^{Max}/P_{in}$ and $\mathrm{FF} = P_{el}^{Max}/I_{sc}V_{oc}$ are also calculated as a function of $P$, as shown in Figure 6c.[27] The maximum PCE and FF can reach 2.79/7.21% and 0.36/0.52 at $V_g$ = 0/−60 V, respectively. This indicates that our fabricated vdWs heterostructure possesses an ultra-high PCE with a lower trapping and recombination rate at the interface. Above all, our fabricated $Bi_2O_2Se/MoTe_2$ heterostructure shows high gate-modulation photovoltaic performance and great potential application in solar cells.

Figure 6d shows $I_{sc}$ relative to the light power density at $V_g$ = −60 and 0 V; the curves are fitted by the power-law equation for $I_{sc} = A \cdot P_{in}^{\alpha}$, where $\alpha$ is the fitting exponent.[11] In summary, $I_{sc}$ increases linearly with increasing light power density. $\alpha$ increases from 0.64 to 0.69, which means that photons absorbed are converted more efficiently into electron−hole pairs at $V_g$ = −60 V under the photovoltaic effect. Meanwhile, $V_{oc}$ scales with $\ln(P_{in})$, as expected from conventional p−n junction theory. The carrier concentration is determined by the balance between the photogenerated carriers ($G \propto P_{in}$) and interlayer recombination rates ($R_a$) under steady-state and open-circuit conditions. The recombination rate can be expressed by the empirical equation[19] $R_a = \gamma \cdot n^{\eta}$, where $\eta$ denotes the recombination order. Generally, monomolecular (Shockley−Read−Hall; SRH) recombination occurs at $\eta$ = 1 and bimolecular (Langevin) recombination occurs at $\eta$ = 2.[46,47] By equating $R_a$ and $G$, the expression is $dV_{oc}/d\ln(P_{in}) = (2K_BT)/\eta q$, which concludes that carrier recombination is dominated by the SRH at $V_g$ = 0 V ($\eta$ = 1.46), while the Langevin recombination process dominates at $V_g$ = −60 V ($\eta$ = 2.08).

To understand the intrinsic charge transport mechanism under gate modulation, the energy band alignment of the heterojunction after contact under irradiation without bias is given. As shown in Figure 6e, due to the different Fermi levels of ambipolar $MoTe_2$ and n$^+$-type $Bi_2O_2Se$, the energy band near the $MoTe_2$ interface becomes downward bending to accommodate the same Fermi energy level, resulting in a built-in electric field with the theoretical type-II staggered band alignment. Therefore, the dark current can be suppressed to as low as 0.98 pA at zero bias. Under 405 nm laser illumination, a large number of photogenerated carriers can be excited in both $MoTe_2$ and $Bi_2O_2Se$ sides, subsequently separating efficiently without the potential barrier through band edge transport by the built-in electric field with a strong interlayer coupling


https://doi.org/10.1021/acsami.3c01807
ACS Appl. Mater. Interfaces 2023, 15, 18101−18113

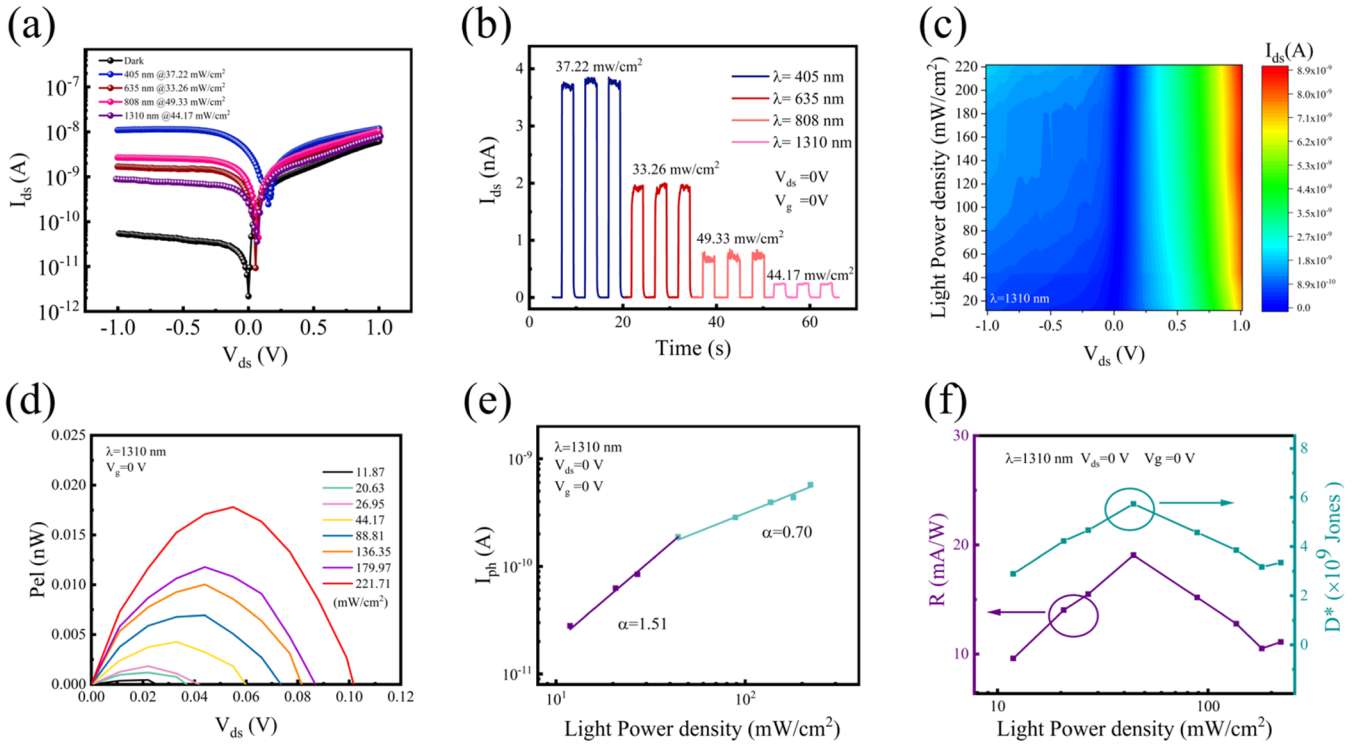


**Figure 7.** Broadband response and near-infrared photovoltaic performance of the $Bi_2O_2Se/MoTe_2$ vdWs photodetector without gate voltage: (a) $I_{ds}-V_{ds}$ characteristics at the logarithmic scale in the dark and under various wavelengths. (b) Time-dependent photoresponse curves of the $Bi_2O_2Se/MoTe_2$ heterojunction photodetector under various wavelengths. (c) 2D false-color photocurrent plot under $\lambda$ = 1310 nm. (d) Output electrical power as a function of $V_{ds}$ under $\lambda$ = 1310 nm at various light power densities. (e) Light power density dependence of $I_{ph}$ under $\lambda$ = 1310 nm. (f) $R$ and $D^*$ as a function of light power density under $\lambda$ = 1310 nm.

effect. A large $I_{light}/I_{dark}$ ratio over $10^4$ at $V_{ds}$ = 0 V can be achieved because of high photosensitivity. Moreover, Figure 6f presents the energy band alignment at $V_g$ = −60 V. Benefiting from the p-dominated ambipolar conductivity characteristics of individual $MoTe_2$ (see Figure S5), the band bending near the $MoTe_2$ interface becomes more and more abrupt because of the obvious movement of the Fermi level for $MoTe_2$ close to the VBM, while the Fermi level of $Bi_2O_2Se$ is basically reserved and provides high electron mobility owing to the heavily n-doping type. Above all, the heterojunction type changes from the n−n$^+$ junction to the p−n$^+$ junction at $V_g$ = −60 V. It is confirmed that the generation, collection, and separation efficiency of the photogenerated carriers can be enhanced, and the dark current can be further suppressed to 0.6 pA across such a large potential difference.[46] In addition, as shown in Figures S11 and S12, to provide the statistics of device characteristics, the other two devices at similar thicknesses are also investigated under 405 nm illumination. It is confirmed that the calculated photovoltaic $R$ at a range of 1.12 + 0.19 A W$^{-1}$ and all the maximum $D^*$ are in the range of $10^{11}$ Jones. The $I_{light}/I_{dark}$ ratios for devices I, II, and III at $P$ = 26.87 mW cm$^{-2}$ are 4.68 × $10^3$, 2.90 × $10^3$, and 3.96 × $10^3$, respectively. Most importantly, the maximum PCE and FF of devices II and III at $V_g$ = 0 V are 5.02 and 0.18% and 3.26 and 0.28%, respectively. Above all, the photovoltaic performance of devices II and III is similar to that of Device I. This indicates that the $Bi_2O_2Se/MoTe_2$ vdWs heterostructure shows good repeatability at similar thicknesses, and it is believed that the photovoltaic performance can also be enhanced with back-gate modulation.

To highlight the advantage of the narrow band gap and near-infrared light absorption efficiency of $Bi_2O_2Se$ in this type-II band alignment, the optoelectrical properties from the visible to near-infrared range without $V_g$ are also investigated. The $I_{ds}-V_{ds}$ curves at the logarithmic scale in the dark and under different wavelengths are illustrated in Figure 7a. Obviously, it exhibits significant photovoltaic and photoconductive behavior under the 405−1310 nm range. The optimal wavelength is obviously 405 nm because of the high light absorption efficiency of the top 2H-$MoTe_2$ layer. Meanwhile, as shown in Figure 7b, rapid and stable photoswitching on/off curves are demonstrated at zero bias under the 405−1310 nm range. In summary, the remarkable photovoltaic effect of the $Bi_2O_2Se/MoTe_2$ photodiode provides a platform for broadband self-driven photodetection. Subsequently, the self-driven photovoltaic performance in a short-wave infrared regime is investigated in depth. Figure 7c shows a 2D false-color plot of the photocurrent under 1310 nm laser irradiation with various light power densities. It can be explained by the moderate light absorption efficiency for $Bi_2O_2Se$ and $MoTe_2$ and the strong coupling effect across a wide depletion region. As shown in Figure 7d, $P_{el}$ reaches its maximum value of 18 pW at $V_{ds}$ = 58 mV when $P$ = 221.71 mW cm$^{-2}$. Figure S10a,b demonstrates that both $V_{oc}$ and $I_{sc}$ increase monotonically as a function of light power density, indicating that a good photovoltaic effect dominates the near-infrared photocurrent generation. On the other hand, we also calculated the important indicators of FF and PCE. From Figure S10c, a maximum FF of 0.23 and PCE up to 0.04% under 1310 nm were obtained for the $Bi_2O_2Se/MoTe_2$ heterostructure. The periodic switching photocurrent without severe degradation


https://doi.org/10.1021/acsami.3c01807
ACS Appl. Mater. Interfaces 2023, 15, 18101−18113

(Figure S10d) ensures good stability and reproducibility of the photovoltaic response in near-infrared light.

Importantly, Figure 7e illustrates the relationship between photocurrent and light power density. In particular, $\alpha$ = 1.51 (super-linear) and $\alpha$ = 0.70 (sub-linear) are obtained under weak and strong light power densities for 1310 nm illumination instead of 405 nm, respectively. Under weak illumination, a small number of carriers are generated, and some of them are trapped by the high-gain trap states.[9] As a result, electrons and holes hardly recombine, leading to a super-linear behavior in $I_{sc}$. At stronger illumination, the sub-linear behavior originates from the reduced nonradiative recombination probability of photogenerated carriers due to fewer trap states, causing the decrease of responsivity. Figure 7f illustrates $R$ and $D^*$ curves as a function of laser power density, with a maximum $R$ of 19 mA·W$^{-1}$ and a $D^*$ of 5.72 × 10$^9$ Jones at $P$ = 44.17 mW cm$^{-2}$ obtained under 1310 nm light, which is comparable to the recently reported BP/$Bi_2O_2Se$ heterostructure.[6,48]

The comparison of performance between our $Bi_2O_2Se$/$MoTe_2$ heterostructure with individual $Bi_2O_2Se$ and other reported 2D vdWs heterostructures is shown in Table S1. Compared with the individual 2D $Bi_2O_2Se$ photodetector, the dark current of our $Bi_2O_2Se$/$MoTe_2$ photodiode is greatly suppressed by 3 orders of magnitude, and the $I_{light}/I_{dark}$ ratio is pronounced, which is important for low-power consumption and high sensitivity in practical applications. Interestingly, the photovoltaic performance under 405−1310 nm is excellent and can be further modulated by $V_g$ because of the ambipolar characteristics of 2H-$MoTe_2$, the effective built-in electric field at the $Bi_2O_2Se$/$MoTe_2$ interface, the narrow band gap of $Bi_2O_2Se$, and designed type-II staggered band alignment with barrier-free band transport.

## 3. CONCLUSIONS

In summary, we constructed a vdWs heterojunction based on the CVD synthesized n$^+$-$Bi_2O_2Se$ and exfoliated ambipolar 2H-$MoTe_2$ by the dry transfer method. DFT calculation illustrates that the bulk $Bi_2O_2Se$/$MoTe_2$ heterojunction forms a type-II energy band arrangement. The electrical verification shows that $Bi_2O_2Se$/$MoTe_2$ possesses an n$^+$−n junction and can be regulated to an n$^+$−p junction at $V_g$ = −60 V. It is demonstrated that DT is the main mechanism of electron flow across the heterojunction under forward/backward bias. As a self-driven phototransistor, the photodetector shows a maximum $R$ of 1.24 A·W$^{-1}$ and a $D^*$ of 3.73 × 10$^{11}$ Jones under 405 nm illumination. The gate modulation allows a large band bending to be formed across the interface; the $R$, FF, PCE, and $D^*$ values can be enhanced to 4.96 A·W$^{-1}$, 0.52, 7.21%, and 3.84 × 10$^{12}$ Jones at $V_g$ = −60 V, respectively. This provides more possibilities for logic optoelectronic applications. Furthermore, the device also realizes broad-spectrum photodetection in the range of 405−1310 nm, showing excellent performance at 1310 nm with a maximum $R$ of 19 mA·W$^{-1}$ and a $D^*$ of 5.72 × 10$^9$ Jones. Considering its ease of fabrication and ultra-high performance, the $Bi_2O_2Se$/$MoTe_2$ heterojunction extends the potential of $Bi_2O_2Se$ for self-driven, high sensitivity, broadband response, and logic optoelectronic applications.

## 4. EXPERIMENTAL SECTION

**4.1. CVD Synthesis of $Bi_2O_2Se$ and Device Fabrication of 2D $Bi_2O_2Se$/$MoTe_2$ Heterostructures.** 2D $Bi_2O_2Se$ was first synthesized on mica by the CVD method, in which the $Bi_2O_3$ powder source and $Bi_2Se_3$ powder (3:1) were placed at the hot center and 6 cm upstream of the tube furnace, and the mica substrate was placed 12−15 cm downstream. The center temperature of the tube furnace was set to about 680−750 °C, with a heating time of about 30 min and a holding time of 25 min, and finally cooled naturally to room temperature. Prior to heating, the quartz tube was evacuated of ambient contamination using high-purity Ar gas at high flow rates and then used as a carrier gas for 200 sccm throughout the growth process.

**4.2. $Bi_2O_2Se$ Transfer from Mica to the $SiO_2$/Si Substrate (Figure S13).** PS was first spin-coated on the surface of f-mica and then baked at 80 °C for 15 min. Then, the PS film was peeled off from the f-mica together with $Bi_2O_2Se$ with the help of deionized water. The PS film was then placed on the Si substrate and baked at 70 °C for 1 h. Finally, it was washed off with toluene, leaving the $Bi_2O_2Se$ sample on the Si substrate. The more hydrophobic surface properties of the PS film and the harder film properties distinguish it from the A10 PMMA film bought from Taizhou SUNANO New Energy Co., Ltd, which makes it easier to be peeled off from the f-mica substrate. 2H-$MoTe_2$ nanosheets were stripped from the bulk single crystal (2D semiconductor Co., Ltd. bought from Shanghai Onway Technology Co., Ltd.) using 3M scotch tape and transferred to the 300 nm $SiO_2$/Si substrate. Subsequently, 2H-$MoTe_2$ nanosheets were stacked onto the top of $Bi_2O_2Se$ nanosheets prepared on $SiO_2$/Si substrates using a PVA/PDMS dry transfer method via a 3D transfer stage (Shanghai Onway Technology Co., Ltd.). Finally, Cr/Au (10/50 nm) contact electrodes were prepared using a positive photoresist of AR-P 5350 and a developing solution of AR 300-26 (ALLRESIST GmbH Company bought from Taizhou SUNANO New Energy Co., Ltd), an Ultraviolet Maskless photolithography machine (TuoTuo Technology (Suzhou) Co., Ltd.), and electron beam deposition techniques.

**4.3. Characterization and Measurement.** The morphology and crystal structure of the $Bi_2O_2Se$/$MoTe_2$ nanosheets were characterized with an optical microscope (ECLIPSE LV150N, Nikon), X-ray diffraction (PANalytical Empyrean), high-resolution transmission electron microscopy (HRTEM), and energy spectrum EDS (JEOL-2100F). The thickness and surface potential difference were measured by AFM and KPFM (Dimension Fast Scan from Bruker Co., Ltd), respectively. Raman spectra were obtained using a confocal microscope spectrometer (Nost Technology Co., Ltd, with a laser excitation of 532 nm and spot diameter of 1−2 $\mu$m). The electrical and optical characteristics were measured by using a four-probe stage equipped with a semiconductor device analyzer (Keithley 2636B) and a four-channel Fiber Coupling Laser system. All of the measurements were performed in ambient conditions.

## ■ ASSOCIATED CONTENT

### Supporting Information

The Supporting Information is available free of charge at https://pubs.acs.org/doi/10.1021/acsami.3c01807.

Details of the DFT; details of the KPFM; analysis of the EDS results of $Bi_2O_2Se$; typical OM image of the as-synthesized 2D $Bi_2O_2Se$ nanoplates on $SiO_2$/Si and low-magnification TEM electron microscopy images of $Bi_2O_2Se$; low-magnification TEM electron microscopy images of $MoTe_2$; HRTEM image of the $MoTe_2$ nanoplate; UPS results of $MoTe_2$ and $Bi_2O_2Se$; output characteristics of individual $MoTe_2$ and $Bi_2O_2Se$; transfer curve of the intrinsic $MoTe_2$ device in linear coordinates; DT plot extracted from Figure 5b; time-dependent photoresponse under on/off switching lasting more than 160 cycles at $V_g$ = 0 and −60 V; $Bi_2O_2Se$/$MoTe_2$ heterojunction photoresponse behavior at different bias; response properties of the $Bi_2O_2Se$/$MoTe_2$ vdWs photodiode under 405 nm illumination; dark current and $S_n$ as a function of frequency at $V_{ds}$ = 0 V, $V_g$



https://doi.org/10.1021/acsami.3c01807
ACS Appl. Mater. Interfaces 2023, 15, 18101−18113

= 0 and −60 V for the $Bi_2O_2Se/MoTe_2$ vdWs photodiode; $I_{ds}$−$V_{ds}$ characteristics, extracted $I_{sc}$ and $V_{oc}$, FF, and PCE under 1310 nm irradiation as a function of laser power intensity under 1310 nm; time-resolved photovoltaic response of the heterostructure under 1310 nm at $V_{ds}$ = 0 V; photoelectrical properties of devices II and III; schematic diagram of $Bi_2O_2Se$ transfer from the mica substrate to the $Si/SiO_2$ substrate; and comparison of photodetection performance in 2D and heterojunction-based detectors (PDF)

## AUTHOR INFORMATION


### Corresponding Authors

**Wei Gao** − *Guangdong Provincial Key Laboratory of Chip and Integration Technology, School of Semiconductor Science and Technology, South China Normal University, Foshan 528225, P. R. China;* orcid.org/0000-0002-8159-3957; Email: gaowei317040@m.scnu.edu.cn

**Lixiang Han** − *Guangdong Provincial Key Laboratory of Chip and Integration Technology, School of Semiconductor Science and Technology, South China Normal University, Foshan 528225, P. R. China*; Email: 20210430@m.scnu.edu.cn

**Jingbo Li** − *Guangdong Provincial Key Laboratory of Chip and Integration Technology, School of Semiconductor Science and Technology, South China Normal University, Foshan 528225, P. R. China*; Email: jbli@m.scnu.edu.cn

### Authors

**Zhiying Dan** − *Guangdong Provincial Key Laboratory of Chip and Integration Technology, School of Semiconductor Science and Technology, South China Normal University, Foshan 528225, P. R. China; Zernike Institute for Advanced Materials, University of Groningen, Groningen 9747AG, The Netherlands*

**Baoxiang Yang** − *Guangdong Provincial Key Laboratory of Chip and Integration Technology, School of Semiconductor Science and Technology, South China Normal University, Foshan 528225, P. R. China*

**Qiqi Song** − *School of Materials and Energy, Guangdong University of Technology, Guangzhou 510006, P. R. China*

**Jianru Chen** − *Guangdong Provincial Key Laboratory of Chip and Integration Technology, School of Semiconductor Science and Technology, South China Normal University, Foshan 528225, P. R. China*

**Hengyi Li** − *Guangdong Provincial Key Laboratory of Chip and Integration Technology, School of Semiconductor Science and Technology, South China Normal University, Foshan 528225, P. R. China*

**Le Huang** − *School of Materials and Energy, Guangdong University of Technology, Guangzhou 510006, P. R. China;* orcid.org/0000-0003-3189-2171

**Menglong Zhang** − *Guangdong Provincial Key Laboratory of Chip and Integration Technology, School of Semiconductor Science and Technology, South China Normal University, Foshan 528225, P. R. China*

**Mengmeng Yang** − *Guangdong Provincial Key Laboratory of Chip and Integration Technology, School of Semiconductor Science and Technology, South China Normal University, Foshan 528225, P. R. China*

**Zhaoqiang Zheng** − *School of Materials and Energy, Guangdong University of Technology, Guangzhou 510006, P. R. China;* orcid.org/0000-0002-1699-2425

**Nengjie Huo** − *Guangdong Provincial Key Laboratory of Chip and Integration Technology, School of Semiconductor Science and Technology, South China Normal University, Foshan 528225, P. R. China;* orcid.org/0000-0003-2520-6243

Complete contact information is available at: https://pubs.acs.org/10.1021/acsami.3c01807


### Notes

The authors declare no competing financial interest.

## ACKNOWLEDGMENTS

This work was financially supported by the National Natural Science Foundation of China (Nos. 62004071, 11904108, and 62175040), Science and Technology Program of Guangzhou (202103030001), "The Pearl River Talent Recruitment Program" (No. 2019ZT08X639), and Guangzhou Basic and Applied Basic Research Project (20220101440).

## REFERENCES


(1) Fu, Q.; Zhu, C.; Zhao, X.; Wang, X.; Chaturvedi, A.; Zhu, C.; Wang, X.; Zeng, Q.; Zhou, J.; Liu, F.; Tay, B. K.; Zhang, H.; Pennycook, S. J.; Liu, Z. Ultrasensitive 2D Bi2O2Se Phototransistors on Silicon Substrates. *Adv. Mater* **2019**, *31*, No. 1804945.

(2) Gao, F.; Chen, H.; Feng, W.; Hu, Y.; Shang, H.; Xu, B.; Zhang, J.; Xu, C. Y.; Hu, P. High-Performance van der Waals Metal-Insulator-Semiconductor Photodetector Optimized with Valence Band Matching. *Adv. Funct. Mater.* **2021**, *31*, No. 2104359.

(3) Wu, D.; Jia, C.; Shi, F.; Zeng, L.; Lin, P.; Dong, L.; Shi, Z.; Tian, Y.; Li, X.; Jie, J. Mixed-Dimensional PdSe2/SiNWA Heterostructure Based Photovoltaic Detectors for Self-Driven, Broadband Photodetection, Infrared Imaging and Humidity Sensing. *J. Mater. Chem. A* **2020**, *8*, 3632−3642.

(4) Ahn, J.; Kang, J. H.; Kyhm, J.; Choi, H. T.; Kim, M.; Ahn, D. H.; Kim, D. Y.; Ahn, I. H.; Park, J. B.; Park, S.; Yi, Y.; Song, J.; Park, M.-C.; Im, S.; Hwang, D. K. Self-Powered Visible-Invisible Multiband Detection and Imaging Achieved Using High-Performance 2D MoTe2/MoS2 Semivertical Heterojunction Photodiodes. *ACS Appl. Mater. Interfaces* **2020**, *12*, 10858−10866.

(5) Hong, S.; Zagni, N.; Choo, S.; Liu, N.; Baek, S.; Bala, A.; Yoo, H.; Kang, B. H.; Kim, H. J.; Yun, H. J.; Alam, M. A.; Kim, S. Highly Sensitive Active Pixel Image Sensor Array Driven by Large-Area Bilayer MoS2 Transistor Circuitry. *Nat. Commun.* **2021**, *12*, No. 3559.

(6) Liu, X.; Wang, W.; Yang, F.; Feng, S.; Hu, Z.; Lu, J.; Ni, Z. Bi2O2Se/BP van der Waals Heterojunction for High Performance Broadband Photodetector. *Sci. China Inf. Sci.* **2021**, *64*, No. 140404.

(7) Zhao, Q.; Gao, F.; Chen, H.; Gao, W.; Xia, M.; Pan, Y.; Shi, H.; Su, S.; Fang, X.; Li, J. High Performance Polarization-Sensitive Self-Powered Imaging Photodetectors Based on a p-Te/n-MoSe2 van der Waals Heterojunction with Strong Interlayer Transition. *Mater. Horiz.* **2021**, *8*, 3113−3123.

(8) Lu, J.; Zheng, Z.; Yao, J.; Gao, W.; Zhao, Y.; Xiao, Y.; Li, J. 2D In2 S3 Nanoflake Coupled with Graphene toward High-Sensitivity and Fast-Response Bulk-Silicon Schottky Photodetector. *Small* **2019**, *15*, No. e1904912.

(9) Yang, M.; Gao, W.; Song, Q.; Zhou, Y.; Huang, L.; Zheng, Z.; Zhao, Y.; Yao, J.; Li, J. Universal Strategy Integrating Strain and Interface Engineering to Drive High-Performance 2D Material Photodetectors. *Adv. Opt. Mater.* **2021**, *9*, No. 2100450.

(10) Tan, C.; Yin, S.; Chen, J.; Lu, Y.; Wei, W.; Du, H.; Liu, K.; Wang, F.; Zhai, T.; Li, L. Broken-Gap PtS2/WSe2 van der Waals Heterojunction with Ultrahigh Reverse Rectification and Fast Photoresponse. *ACS Nano* **2021**, *15*, 8328−8337.

(11) Lei, T.; Tu, H.; Lv, W.; Ma, H.; Wang, J.; Hu, R.; Wang, Q.; Zhang, L.; Fang, B.; Liu, Z.; Shi, W.; Zeng, Z. Ambipolar Photoresponsivity in an Ultrasensitive Photodetector Based on a WSe2/InSe Heterostructure by a Photogating Effect. *ACS Appl. Mater. Interfaces* **2021**, *13*, 50213−50219.

(12) Fang, F.; Wan, Y.; Li, H.; Fang, S.; Huang, F.; Zhou, B.; Jiang, K.; Tung, V.; Li, L. J.; Shi, Y. Two-Dimensional Cs2AgBiBr6/WS2 Heterostructure-Based Photodetector with Boosted Detectivity via Interfacial Engineering. *ACS Nano* **2022**, *16*, 3985−3993.
(13) Wu, J.; Qiu, C.; Fu, H.; Chen, S.; Zhang, C.; Dou, Z.; Tan, C.; Tu, T.; Li, T.; Zhang, Y.; Zhang, Z.; Peng, L.-M.; Gao, P.; Yan, B.; Peng, H. Low Residual Carrier Concentration and High Mobility in 2D Semiconducting Bi2O2Se. *Nano Lett.* **2019**, *19*, 197−202.
(14) Li, P.; Han, A.; Zhang, C.; He, X.; Zhang, J.; Zheng, D.; Cheng, L.; Li, L. J.; Miao, G. X.; Zhang, X. X. Mobility-Fluctuation-Controlled Linear Positive Magnetoresistance in 2D Semiconductor Bi2O2Se Nanoplates. *ACS Nano* **2020**, *14*, 11319−11326.
(15) Huang, C.; Yu, H. Two-Dimensional Bi2O2Se with High Mobility for High-Performance Polymer Solar Cells. *ACS Appl. Mater. Interfaces* **2020**, *12*, 19643−19654.
(16) Liu, B.; Zhao, Y.; Verma, D.; Wang, L. A.; Liang, H.; Zhu, H.; Li, L. J.; Hou, T. H.; Lai, C. S. Bi2O2Se-Based Memristor-Aided Logic. *ACS Appl. Mater. Interfaces* **2021**, *13*, 15391−15398.
(17) Chen, Y.; Ma, W.; Tan, C.; Luo, M.; Zhou, W.; Yao, N.; Wang, H.; Zhang, L.; Xu, T.; Tong, T.; et al. Broadband Photodetectors: Broadband Bi2O2Se Photodetectors from Infrared to Terahertz (Adv. Funct. Mater. 14/2021). *Adv. Funct. Mater.* **2021**, *31*, No. 2170093.
(18) Wu, J.; Wei, M.; Mu, J.; Ma, H.; Zhong, C.; Ye, Y.; Sun, C.; Tang, B.; Wang, L.; Li, J.; Xu, X.; Liu, B.; Li, L.; Lin, H. High-Performance Waveguide-Integrated Bi2O2Se Photodetector for Si Photonic Integrated Circuits. *ACS Nano* **2021**, *15*, 15982−15991.
(19) Luo, P.; Wang, F.; Qu, J.; Liu, K.; Hu, X.; Liu, K.; Zhai, T. Self-driven $WSe_2/Bi_2O_2Se$ van der Waals heterostructure photodetectors with high light on/off ratio and fast response. *Advanced Functional Materials* **2021**, *31*, 2008351.
(20) Chen, J.; Zhu, J.; Wang, Q.; Wan, J.; Liu, R. Homogeneous 2D MoTe2 CMOS Inverters and p-n Junctions Formed by Laser-Irradiation-Induced p-Type Doping. *Small* **2020**, *16*, No. e2001428.
(21) Zheng, W.; Bonn, M.; Wang, H. I. Photoconductivity Multiplication in Semiconducting Few-Layer $MoTe_2$. *Nano Lett.* **2020**, *20*, 5807−5813.
(22) Ahmed, F.; Shafi, A. M.; Mackenzie, D. M.; Qureshi, M. A.; Fernandez, H. A.; Yoon, H. H.; Uddin, M. G.; Kuittinen, M.; Sun, Z.; Lipsanen, H. Multilayer $MoTe_2$ Field-Effect Transistor at High Temperatures. *Adv. Mater. Interfaces* **2021**, *8*, No. 2100950.
(23) Hong, C.; Tao, Y.; Nie, A.; Zhang, M.; Wang, N.; Li, R.; Huang, J.; Huang, Y.; Ren, X.; Cheng, Y.; Liu, X. Inclined Ultrathin $Bi_2O_2Se$ Films: A Building Block for Functional van der Waals Heterostructures. *ACS Nano* **2020**, *14*, 16803−16812.
(24) Chen, W.; Khan, U.; Feng, S.; Ding, B.; Xu, X.; Liu, B. High-Fidelity Transfer of 2D $Bi_2O_2Se$ and Its Mechanical Properties. *Adv. Funct. Mater.* **2020**, *30*, No. 2004960.
(25) Khan, U.; Tang, L.; Ding, B.; Yuting, L.; Feng, S.; Chen, W.; Khan, M. J.; Liu, B.; Cheng, H. M. Catalyst-Free Growth of Atomically Thin Bi2O2Se Nanoribbons for High-Performance Electronics and Optoelectronics. *Adv. Funct. Mater.* **2021**, *31*, No. 2101170.
(26) Fan, C.; Dai, B.; Liang, H.; Xu, X.; Qi, Z.; Jiang, H.; Duan, H.; Zhang, Q. Epitaxial Growth of 2D $Bi_2O_2Se$ Nanoplates/1D $CsPbBr_3$ Nanowires Mixed-Dimensional Heterostructures with Enhanced Optoelectronic Properties. *Adv. Funct. Mater.* **2021**, *31*, No. 2010263.
(27) Yang, S.; Luo, P.; Wang, F.; Liu, T.; Zhao, Y.; Ma, Y.; Li, H.; Zhai, T. Van der Waals Epitaxy of $Bi_2Te_2Se/Bi_2O_2Se$ Vertical Heterojunction for High Performance Photodetector. *Small* **2022**, *18*, No. e2105211.
(28) Yang, T.; Li, X.; Wang, L.; Liu, Y.; Chen, K.; Yang, X.; Liao, L.; Dong, L.; Shan, C.-X. Broadband Photodetection of 2D $Bi_2O_2Se$−$MoSe_2$ Heterostructure. *J. Mater. Sci.* **2019**, *54*, 14742−14751.
(29) Tao, L.; Yao, B.; Yue, Q.; Dan, Z.; Wen, P.; Yang, M.; Zheng, Z.; Luo, D.; Fan, W.; Wang, X.; Gao, W. Vertically Stacked $Bi_2Se_3/MoTe_2$ Heterostructure with Large Band Offsets for Nanoelectronics. *Nanoscale* **2021**, *13*, 15403−15414.
(30) Xiong, J.; Sun, Y.; Wu, L.; Wang, W.; Gao, W.; Huo, N.; Li, J. High Performance Self-Driven Polarization-Sensitive Photodetectors Based on GeAs/InSe Heterojunction. *Adv. Opt. Mater.* **2021**, *9*, No. 2101017.
(31) Yin, J.; Tan, Z.; Hong, H.; Wu, J.; Yuan, H.; Liu, Y.; Chen, C.; Tan, C.; Yao, F.; Li, T.; Chen, Y.; Chen, Y.; Liu, Z.; Liu, K.; Liu, K.; Peng, H. Ultrafast and Highly Sensitive Infrared Photodetectors Based on Two-Dimensional Oxyselenide Crystals. *Nat. Commun.* **2018**, *9*, No. 3311.
(32) Gao, W.; Zhang, F.; Zheng, Z.; Li, J. Unique and Tunable Photodetecting Performance for Two-Dimensional Layered $MoSe_2/WSe_2$ p-n Junction on the 4H-SiC Substrate. *ACS Appl. Mater. Interfaces* **2019**, *11*, 19277−19285.
(33) Guo, S.; Chen, Z.; Weller, D.; Wang, X.; Ding, C.; Wang, Y.; Liu, R. Toward High-Performance Self-Driven Photodetectors via Multistacking Van der Waals Heterostructures. *ACS Appl. Mater. Interfaces* **2021**, *13*, 56438−56445.
(34) Kim, J.; Venkatesan, A.; Kim, H.; Kim, Y.; Whang, D.; Kim, G. H. Improved Contact Resistance by a Single Atomic Layer Tunneling Effect in $WS_2/MoTe_2$ Heterostructures. *Adv. Sci.* **2021**, *8*, No. e2100102.
(35) Li, S.; Zhang, J.; Zhu, L.; Zhang, K.; Gao, W.; Li, J.; Huo, N. Reconfigurable and Broadband Polarimetric Photodetector. *Adv. Funct. Mater.* **2023**, *33*, No. 2210268.
(36) Han, X.; Wen, P.; Zhang, L.; Gao, W.; Chen, H.; Gao, F.; Zhang, S.; Huo, N.; Zou, B.; Li, J. A Polarization-Sensitive Self-Powered Photodetector Based on a p-$WSe_2$/$TaIrTe_4$/n-$MoS_2$ van der Waals Heterojunction. *ACS Appl. Mater. Interfaces* **2021**, *13*, 61544−61554.
(37) Lopez-Sanchez, O.; Lembke, D.; Kayci, M.; Radenovic, A.; Kis, A. Ultrasensitive Photodetectors Based on Monolayer $MoS_2$. *Nat. Nanotechnol.* **2013**, *8*, 497−501.
(38) Ahn, J.; Kang, J. H.; Park, M. C.; Hwang, D. K. All 2D $WSe_2/MoS_2$ Heterojunction Photodiode and Its Image Sensor Application. *Opt. Lett.* **2020**, *45*, 4531−4534.
(39) Lu, M. Y.; Chang, Y. T.; Chen, H. J. Efficient Self-Driven Photodetectors Featuring a Mixed-Dimensional van der Waals Heterojunction Formed from a CdS Nanowire and a $MoTe_2$ Flake. *Small* **2018**, *14*, No. e1802302.
(40) Yang, B.; Gao, W.; Li, H.; Gao, P.; Yang, M.; Pan, Y.; Wang, C.; Yang, Y.; Huo, N.; Zheng, Z.; Li, J. Visible and Infrared Photodiode Based on $\gamma$-InSe/Ge van der Waals Heterojunction for Polarized Detection and Imaging. *Nanoscale* **2023**, *15*, 3520−3531.
(41) Wu, L.; Gao, W.; Sun, Y.; Yang, M.; Zheng, Z.; Fan, W.; Shu, K.; Dan, Z.; Zhang, N.; Huo, N.; Li, J. Polarity-Switchable and Self-Driven Photo-Response Based on Vertically Stacked Type-III GeSe/$SnS_2$ Heterojunction. *Adv. Mater. Interfaces* **2022**, *9*, No. 2102099.
(42) Zhang, N.; Wu, L.; Gao, W.; Zhao, Q.; Huo, N.; Li, J. Near-Infrared, Self-Powered and Polarization-Sensitive Photodetector Based on GeSe−$MoTe_2$ p−n Heterojunction. *Adv. Mater. Interfaces* **2022**, *9*, No. 2200150.
(43) Lu, J.; Zheng, Z.; Gao, W.; Yao, J.; Zhao, Y.; Xiao, Y.; Wang, B.; Li, J. Epitaxial Growth of Large-Scale $In_2S_3$ Nanoflakes and the Construction of a High Performance In2S3/Si Photodetector. *J. Mater. Chem. C* **2019**, *7*, 12104−12113.
(44) Wen, P.; Zhang, L.; Gao, W.; Yue, Q.; Wang, H.; Huang, Y.; Wu, J.; Yu, H.; Chen, H.; Huo, N.; Li, J. Gate-Tunable Photovoltaic Effect in $MoTe_2$ Lateral Homojunction. *Adv. Electron. Mater.* **2022**, *8*, No. 2101144.
(45) Sun, Y.; Xiong, J.; Wu, X.; Gao, W.; Huo, N.; Li, J. Highly Sensitive Infrared Polarized Photodetector Enabled by Out-of-Plane PSN Architecture Composing of p-$MoTe_2$, Semimetal-$MoTe_2$ and n-$SnSe_2$. *Nano Res.* **2021**, *15*, 5384−5391.
(46) Furchi, M. M.; Pospischil, A.; Libisch, F.; Burgdorfer, J.; Mueller, T. Photovoltaic Effect in an Electrically Tunable van der Waals Heterojunction. *Nano Lett.* **2014**, *14*, 4785−4791.
(47) Rauh, D.; Deibel, C.; Dyakonov, V. Charge Density Dependent Nongeminate Recombination in Organic Bulk Heterojunction Solar Cells. *Adv. Funct. Mater.* **2012**, *22*, 3371−3377.
(48) Chen, Y.; Tan, C.; Wang, Z.; Miao, J.; Ge, X.; Zhao, T.; Liao, K.; Ge, H.; Wang, Y.; Wang, F.; et al. Momentum-Matching and

Band-Alignment van der Waals Heterostructures for High-Efficiency Infrared Photodetection. *Sci. Adv.* **2022**, *8*, No. eabq1781.





https://doi.org/10.1021/acsami.3c01807
*ACS Appl. Mater. Interfaces* 2023, 15, 18101−18113